EES Batteries

PAPER

View Article Online
View Journal | View Issue

Cite this: *EES Batteries*, 2025, **1**, 172

Transport characterization of solid-state Li_2FeS_2 cathodes from a porous electrode theory perspective†

Tim Bernges,*[a] Lukas Ketter,[a,b] Bianca Helm,[c] Marvin A. Kraft,[d] Kimberly A. See[e] and Wolfgang G. Zeier*[a,b,d]

Received 6th September 2024,
Accepted 14th October 2024

DOI: 10.1039/d4eb00005f

rsc.li/EESBatteries

The abundance and cost of resources for current state-of-the-art cathode active materials makes the search for alternative cell chemistries inevitable. Nonetheless, especially in solid-state batteries, establishing new cell chemistries comes at the challenge of optimizing the transport of both charge carriers, electrons and ions, through the electrode. Limitations in transport of either species lead to underutilization of the electrode caused by insufficiently contacted particles and/or nonuniform reaction rates and state-of-charge gradients through the electrode. In this work, we investigate the capabilities of Li_2FeS_2 as alternative active material in all-solid-state cathodes by thorough investigation of the initial utilization and rate capability as a function of the cathode loading. The cathode loading is increased from 1.8 to 7.3 mA h cm^{-2} by increasing the fraction of active material from 32 to 74 vol%, and the thickness of the composite electrode from 73 to 145 μm. Careful characterization of the effective electronic and ionic transport, and consideration of the δ-parameter from porous electrode theory, guides the understanding of the electrode performances. With that, this work shows that Li_2FeS_2 solid-state cathodes with high areal loadings and gravimetric energy densities can be realized.

Broader context

Solid-state batteries are explored to replace lithium-ion batteries soon. However, a move from liquid electrolytes to solid state electrolytes requires the fabrication of all-solid electrodes and with-it optimization of the composition, electrode thickness and applied – as well as possible practical high – current densities. This work uses the active material Li_2FeS_2 as a case study to describe electrode transport by using a descriptor for electrode transport that allows a qualitative characterization of the quality of electrode transport of different active materials, solid electrolyte and additive systems for cathodes and anodes alike in solid-state batteries. Overall, the discussion factors in the thickness of the electrode and the applied current density, therefore setting the results and discussion in context of desired high-energy density electrodes and fast-charging scenarios. This allows a first prediction of the onset of transport limitations when targeting practically desired cell loadings in solid-state batteries.

[a]*Institute of Inorganic and Analytical Chemistry, University of Münster, D-48149 Münster, Germany. E-mail: tbernges@uni-muenster.de, wzeier@uni-muenster.de*
[b]*International Graduate School for Battery Chemistry, Characterization, Analysis, Recycling and Application (BACCARA), University of Münster, D-48149 Münster, Germany*
[c]*Bavarian Center for Battery Technology (BayBatt), University of Bayreuth, D-95447 Bayreuth, Germany*
[d]*Institute of Energy Materials and Devices (IMD), IMD-4: Helmholtz-Institut Münster, Forschungszentrum Jülich, 48149 Münster, Germany*
[e]*Division of Chemistry and Chemical Engineering, California Institute of Technology, Pasadena, 91125 California, USA*

†Electronic supplementary information (ESI) available: Synthesis details and structural characterization, chronoamperometry and transmission-line modelling of impedance spectra, details of effective-medium modelling, additional information and depictions regarding the electrochemical characterization. See DOI: https://doi.org/10.1039/d4eb00005f

Introduction

Li-ion batteries pose an integral part of todays energy economics but are expected to run into limitations of achievable energy density in the future, motivating the investigation of different technologies, *e.g.*, solid-state batteries.[1,2] In both, conventional Li-ion and solid-state batteries, the layered oxides $LiNi_{1-x}Mn_yCo_{1-x-y}O_2$ (NCM) are the most utilized and thoroughly investigated cathode active material.[3] Nonetheless, among other things, the relative scarcity of Co and Mn, and resulting material costs make the search for alternatives a promising endeavour.[4–6] The cathode active material Li_2FeS_2 offers a cost-effective alternative given the large abundance of both iron and sulfur,[4] comparable to the promised benefits of

other alternative chemistries such as $LiFePO_4$ (LFP) and Li–S.[7,8] At the same time, moving from NCM to Li_2FeS_2 means higher mechanical compatibility, and moving from high- to low-potential electrodes promises better alignment with the stability window of the state-of-the-art sulfur-based solid-electrolytes.[9]

In addition to these benefits, Li_2FeS_2 on paper offers a two electron reaction following full delithiation from Li_2FeS_2 to FeS_2. Considering this range, the theoretical capacity of Li_2FeS_2 amounts to 400 mA h g^{-1}, exceeding the theoretical capacity of NCM811 that is ≈280 mA h g^{-1} but coming at the disadvantage of a lower potentials of operation. Nonetheless, Hansen and coworkers[10] recently proposed that the reaction is limited to the chemical space between Li_2FeS_2 and $Li_{0.5}FeS_2$ relating to a theoretical capacity of 300 mA h g^{-1} in the investigated voltage range, as corroborated by other reports.[11] This conclusion is reached by state-of-charge dependent characterizations using *in situ* X-ray diffraction as well as *ex situ* Fe and S K-edge XANES experiments.[10] The proposed reaction mechanism is as follows:[10,12,13] first the delithiation of Li_2FeS_2 to $Li_{1.5}FeS_2$ is charge balanced by the oxidation of Fe^{2+} to Fe^{3+}. At the nominal composition $Li_{1.5}FeS_2$, an ordering of the $Fe^{2+/3+}$ and Li^+ substructure occurs. Further delithiation takes place in a two-phase regime between $Li_{1.5}FeS_2$ and $Li_{0.5}FeS_2$, where charge is balanced by sulfur dimer formation, *i.e.*, the formal oxidation of S^{2-} to $(S_2)^{2-}$. In $Li_{0.5}FeS_2$, half of all sulfur ions are dimerized and further delithiation faces a large energetic barrier. This is in agreement with the computational work by Wei *et al.*[14] that suggests that while further delithiation from $Li_{0.5}FeS_2$ to FeS_2 is hindered by a significant increase of the formation enthalpies, it may be achieved if the potential barrier is overcome.

While the cathode active material Li_2FeS_2 has been successfully utilized in Li-ion batteries using organic liquid electrolytes,[10,12] its potential for solid-state batteries is scarcely investigated to date.[15,16] The transition from porous electrodes infiltrated with liquid electrolyte to solid-state cathodes means the change to solid–solid cathode composites containing cathode active material (CAM) and solid electrolyte (SE). With that the question of the optimal mixing ratio of both components arises. From a transport perspective, the mixing (volumetric) ratio determines the effective ionic and electronic conductivity in and through the cathode composite to a major extent. With electrochemical reactions requiring both charge carriers, sufficiently fast transport of both through the entire thickness of the cathode is necessary for high cathode utilization.[17–19] Generally, electronic conductivity is contributed by either the CAM itself or by conductive additives,[17,20] such that the effective electronic conductivity increases with the volume fraction of CAM in the composite. Opposed to that, the effective ionic transport mainly provided by the SE increases with its volume fraction and consequently decreases with the CAM fraction in the composite.[17] This interdependence of both conductivities on the volumetric ratio of the components makes optimizing cathode composite transport a challenging task.[21]

The situation is further complicated by the general goal of designing high energy density cathodes that are feasible for application. An increase of the energy density of the cathode, or its areal loading (in units of mA h cm^{-2}), can be achieved by increasing the CAM volume fraction given the simultaneous reduction of formaly electrochemically inactive SE.[3] The increase of the CAM fraction leads to an increase in the effective electronic conductivity of the composite but has detrimental influence on the effective ionic conductivity.[17] This leads to the system being ion transport limited, *i.e.*, to insufficiently fast ion transport, when going to the desired high volume fractions of CAM. Underutilization of the cathode and saturation or decline of the achievable energy density follow.[21] The saturation behavior can be understood considering that increasing the areal loading above a threshold of the CAM volume fraction leads to a significant loss in cathode utilizations and a net-zero win in achievable energy density. This trend is schematically depicted in Fig. 1 (red shading). Various examples of ionic transport limitations leading to cathode underutilziation can be found in literature, *e.g.*, for Li_6PS_5Cl–Graphite anode composites,[20] in Li–S solid-state cells,[19] and in Li_6PS_5Cl–$LiNi_{0.6}Co_{0.2}Mn_{0.2}O_2$ cathodes.[17]

Nonetheless, the energy density of the cathode can be increased above this threshold by increasing the cathode thickness (schematically depicted in Fig. 1, blue shading).[3] But, the increase in cathode thickness can amplify and exacerbate already existing transport limitations at medium to high CAM fraction again limiting the achievable energy densities. This can be intuitively understood by the elongated conduction paths for both charge carriers, that require even faster effective transport through the electrode. In agreement with this viewpoint, Kato and coworkers[18] reported on a decrease of the cathode utilization in $LiCoO_2$–$Li_{10}GeP_2S_{12}$ cathodes when increasing the cathode thickness and simulations on a com-

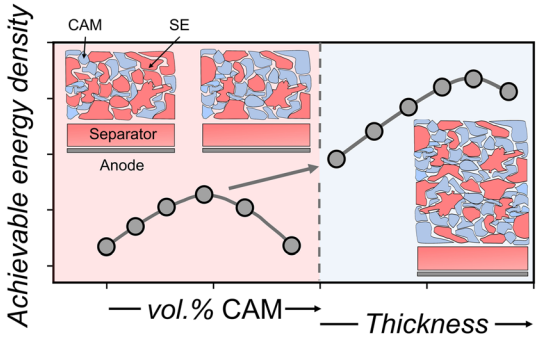

Fig. 1 Schematic representation of strategies to increase the energy density considering only the configuration of the cathode. On a composite-composition level, first the energy density can be significantly increased by increasing the volume fraction of electrochemically active material (vol% CAM). A maximum is reached given the onset of transport limitations. At this stage, further increase of the energy density can be achieved by increasing the thickness of the cathode. Nonetheless, increasing the electrode thickness further amplifies transport limitations that are decisive for the maximum achievable energy density.

parable system using Li_3PS_4 as SE indicate that reaction fronts and state-of-charge gradients are the underlying reasons.[22]

In this work, we investigate the solid-state cathode system $Li_{5.5}PS_{4.5}Cl_{1.5}$ (SE)–Li_2FeS_2 (CAM) with varying volume fractions of CAM to identify potential onsets of kinetic limitations. This is done by evaluating the effective conductivities using chronoamperometry, impedance spectroscopy, and effective medium modelling. Successively, the influence on cathode utilization is investigated and related to the transport characteristics of the system. The porous electrode theory developed by Newman and Tobias[23] is revisited and a dimensionless descriptor identified to describe transport limitations of the system. This descriptor is used to qualitatively guide the understanding of our results. From this, it is shown that high volume fraction CAM cathodes can be realized that show good cathode utilization at low applied current densities even when aiming for thicker electrodes. Nonetheless, lower rate capability at higher applied current densities is a consequence of increasing the cathode loading, *i.e.*, the cathode energy density. With that, this work shows the general capabilities of Li_2FeS_2 as CAM in solid-state batteries and reveals limitations in the field of solid-state batteries in general that have to be targeted by future research.

Experimental section

Sample preparation

Cathode composites of Li_2FeS_2 and $Li_{5.5}PS_{4.5}Cl_{1.5}$ were prepared using a shaker mill with a frequency of 15 Hz for five minutes. Synthesis details and quality control of the synthesized materials are given in the ESI (Fig. S1, Tables S1 and S2†). The ZrO_2 shaker mill cup (15 mL) was filled with 200 mg of a Li_2FeS_2 and $Li_{5.5}PS_{4.5}Cl_{1.5}$ mixture in the targeted volumetric ratio. Composites with Li_2FeS_2 volume fractions of 0.32, 0.41, 0.51, 0.62 and 0.74 were prepared corresponding to weight fractions of 0.4, 0.5, 0.6, 0.7 and 0.8. Twenty 3 mm ZrO_2 milling media were filled in the shaker cup for the processing. Sample handling and preparation was exclusively done under inert atmosphere in an Ar-filled glovebox.

Partial transport characterization

Two techniques were employed to evaluate the partial conductivities of the composites. The electronic conductivity was exclusively measured by chronoamperometry in electron conducting/ion blocking conditions, created by placing the sample between stainless steel current collectors. The ionic conductivity is determined in electron-blocking but ion conducting conditions by stacking SE and In/LiIn symmetrically on both sites of the sample. The polarization experiments were performed in a range of −45 mV to 50 mV, and 1 mV to 8 mV, for the electronic and ionic conductivity, respectively. All raw data and details of the data evaluation are given in the ESI.† Potentiostatic impedance spectroscopy was conducted to corroborate the partial ionic conductivity of the composites. The spectra were collected in a half cell configuration of In/LiIn|$Li_{5.5}PS_{4.5}Cl_{1.5}$|Li_2FeS_2/$Li_{5.5}PS_{4.5}Cl_{1.5}$. The investigated frequency range was 7 MHz to 50 mHz, with 25 sampled frequencies per decade using an excitation amplitude of 10 mV. The response was analyzed using a Z-type transmission-line model. Simultaneous determination of the partial electronic conductivities could not be done reliably. This is, because the significantly lower resistance contributions lead to increased uncertainties during fitting. Thus, the electronic resistance where fixed to the expected value from chronoamperometry to stabilize the fitting procedure. Details of the data evaluation are given in the main text and the ESI.†

Electrochemical characterization

Half-cells were constructed using 12 mg Li_2FeS_2/$Li_{5.5}PS_{4.5}Cl_{1.5}$ cathode composites (≈73–85 μm), 80 mg of $Li_{5.5}PS_{4.5}Cl_{1.5}$ separator and a In/LiIn anode (In-foil towards separator, Li-foil towards current collector) in a press cell setup (10 mm diameter) with stainless steel current collectors.[24] The separator and composite are densified at a pressure of 370 MPa before application of the anode. The relative densities of the composite layer are in the range of 85 ± 3% independent of composition. The anode is prepared by first placing In-foil (ChemPur, 0.1 mm, 99.999%) on the separator, followed by Li foil that has been freshly prepared from a Li rod (abcr GmbH, 99.8%). For the evaluation of thicker electrodes, the cathode mass was increased to 18 and 24 mg. All cells were cycled at a controlled temperature of 298 K with an applied pressure of 40 MPa and with a rate of 0.134C (assuming theoretical capacity 300 mA h g^{-1}). The rate capability was characterized by cycling the cells for five cycles at step-wise increasing current densities starting from 0.134C (≈0.24 to 0.98 mA cm^{-2}) going to a maximum applied current density of 5.1 mA cm^{-2}. An overview of all applied current densities in terms of C-rate and the approximated cathode thicknesses is given in Table S3 of the ESI.†

Results and discussion

Porous electrodes in (solid-state) batteries

Extensive work has been done in the past to theoretically describe the electrochemical behavior of electrodes that consist of a porous, electron conducting active material (matrix) infiltrated by ion conducting liquid electrolyte.[23,25,26] The theory of porous electrodes aims to describe the spatial distribution of current densities and reaction rates throughout the electrode that depend on the electrode geometry, the effective electronic and ionic conductivity, and the polarization behavior of the active material. These distributions, if nonuniform, can be considered the underlying reason for cathode underutilization, or the creation of state-of-charge gradients over the electrode. Not considered specifically in the porous electrode theory, the approximations commonly made to the solvent-based electrolyte, *e.g.*, no concentration gradients, neglecting electrochemical double-layer formation and dismissing convection, are fulfilled in SE.[27] Consequently, the

results of the porous electrode theory should persist to the solid-state configuration.

Newman and Tobias[23] derived a description of reaction current distributions through the electrode in one dimension. In the one-dimensional approximation, the current densities and reaction rates are only a function of the relative position x in the electrode located between the separator (x = 0) and the current collector (x = L) interface (schematically shown in Fig. 2, left). The electronic current density i_e in the active material and ionic current density i_{ion} in the electrolyte are described by Ohms law:[23,28]

$$i_e = -\sigma_e \frac{d\varphi_{AM}}{dx} \quad \text{and} \quad i_{ion} = -\sigma_{ion} \frac{d\varphi_{El}}{dx}, \tag{1}$$

where σ_e and σ_{ion} denote the effective electronic and ionic conductivity, and φ_{AM} and φ_{El} the electric potential in the active material and (solid) electrolyte, respectively. Furthermore, charge is conserved thus that:

$$\frac{di_e}{dx} + \frac{di_{ion}}{dx} = 0. \tag{2}$$

In the model, it is assumed that charge is transferred exclusively between the electrolyte and active material at their interface. Charge transfer is a function of the polarization at the active material–electrolyte interface, given by the general form of:

$$\frac{di_e}{dx} = a \cdot f(|\varphi_{AM} - \varphi_{El}|), \tag{3}$$

where a represents the specific (CAM-SE) interfacial area and $f(|\varphi_{AM} - \varphi_{El}|)$ is any suitable function to describe the polarization at the interface as a function of the potential difference $|\varphi_{AM} - \varphi_{El}|$.[23] The function can take the general form of the Butler–Volmer equation, a linearized approximation for low overpotentials and a Tafel approximation for high overpotentials of charge transfer.[29]

Newman and Tobias[23] showed that this set of equations can be cast into a differential equation to describe the reaction current density distribution. The differential equation can be solved numerically using appropriate boundary conditions. From this assessment, dimensionless descriptors were identified that scale with and give a measure of the uniformity of the reaction current density distribution. For Tafel polarization and considering symmetric charge transfer coefficients in the polarization equation, the uniformity of the reaction current density distribution is proportional to a dimensionless current density δ:[23,27]

$$\delta = L \cdot |i| \cdot \frac{0.5 \cdot n_e \cdot F}{R \cdot T} \cdot \left(\frac{1}{\sigma_e} + \frac{1}{\sigma_{ion}}\right), \tag{4}$$

where $i = i_{ion} + i_e$ is the total applied current density, n_e is the number of electrons partaking in the reaction and L is the thickness of the electrode. The dimensionless current density describes the relative ratio of Ohmic potential losses in the cathode to limitations by (slow) reaction kinetics. For low values of $\delta \lesssim 1$, the reaction current density distribution is uniform and the kinetics of the reaction, *i.e.*, the exchange current density, limit the system. This is the case for high effective conductivities and $\sigma_{ion} \approx \sigma_e$ low applied current densities and in thin electrode configuration (blue line in Fig. 2a, right). In contradistinction, Ohmic potential losses are dominant and result in nonuniform reaction current densities for high values of $\delta \gg 1$. High values of δ are a result of low effective conductivities, high applied current densities and increasing the electrode thickness. If the effective electronic conductivity is significantly higher compared to its ionic analogue, *i.e.*, $\sigma_{ion} \ll \sigma_e$ the reaction in the composite preferably takes place at the interface to the separator where ions are supplied from (red line in Fig. 2a, left). *Vice versa*, in the case of $\sigma_{ion} \gg \sigma_e$ reaction rates are higher at the current collector interface from where electrons are supplied. The spatial preference

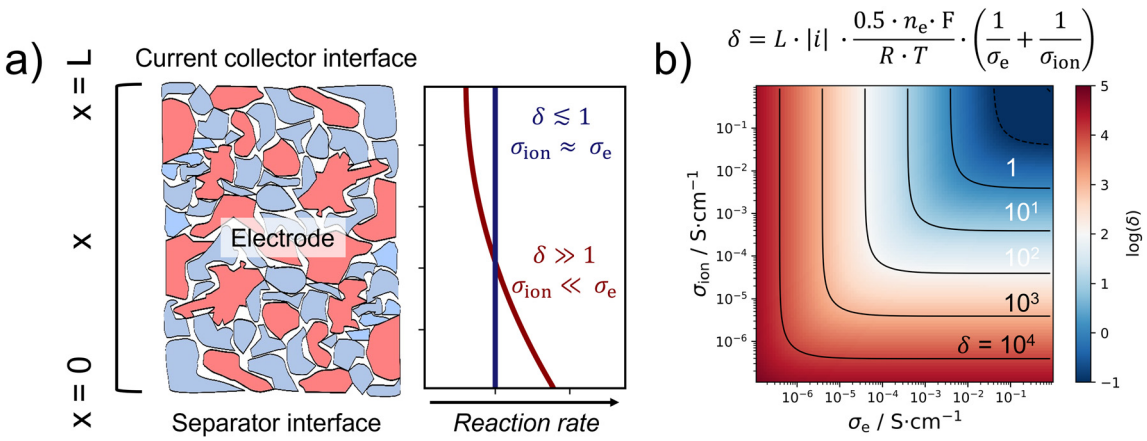

Fig. 2 (a, left) Schematic of a cathode composite with length L consisting of an active material (blue) and a solid electrolyte (red). The relative position within the cathode in porous electrode theory x is defined between the cathode-separator interface (x = 0) and the current collector interface (x = L). (right) Schematic depiction of uniform reaction rate distributions (blue, $\delta \lesssim 1$ and $\sigma_{ion} \approx \sigma_e$ and for reaction rate distributions that are significantly limited by ionic transport ($\delta \gg 1$ and $\sigma_{ion} \ll \sigma_e$). (b) The δ-parameter as a function of the effective conductivities at a constant thickness and current density (L = 200 μm, i = 5 mA cm^{-2}). Contour lines highlight the magnitude of δ.

of reactions due to imbalance of the effective ionic and effective electronic transport ultimately leads to reaction fronts that have been experimentally shown to exist in both lithium–sulfur[19] and NCM-based solid-state batteries.[30]

Considering that both, the thickness and the applied current density are desired to be high to improve energy density and enable fast charging, the conductivity term is the free composite design parameter for achieving low values of δ. The δ-parameter as a function of both effective conductivities is shown in Fig. 2b for an exemplary thickness of 200 μm and a current density of 5 mA cm^{-2}. It shows that the δ-parameter is low, and reaction rates are uniform, when both conductivities are high and equal (diagonal in Fig. 2b). When one effective conductivity is significantly lower than its counterpart, δ is high (lower and left boundaries in Fig. 2b). With that, the uniformity of the reaction rate distribution, inversely proportional to δ, is limited by the lower conductivity. Exemplarily, this means that changing σ_e in the situation $\sigma_{ion} \ll \sigma_e$, while keeping σ_{ion} constant, does not lead to significant changes in δ until the condition $\sigma_{ion} \approx \sigma_e$ is reached (staying on the contour lines in Fig. 2b). Opposed to that, changing σ_{ion} in the same case has drastic influences ("moving" perpendicular to contour lines in Fig. 2b). By changing the volume fractions of electrolyte and active material or the microstructure of the composite, both conductivities of the porous electrode change simultaneously, complicating this assessment.

In this work, we consider the δ-parameter as stated by Newman and Tobias.[23,27] Nonetheless, similar descriptors are derived by Wagner,[28] Micka[25] and Euler and Nonnenmacher[26] treating either specific electrode cases or considering different polarization equations. In the following, we evaluate the potential of the δ-parameter as a qualitative descriptor to guide the design of solid-state battery electrodes by investigating the transport and performance of cathode composites with changing SE to CAM volume ratio, changing thickness and applied current density.

Effective conductivities of the cathode composites

Characterization of transport in cathode composites is important for the understanding and improvement of cathode utilization, both, proposed by the δ-parameter analysis (Fig. 2b and eqn (6)), and shown experimentally for various solid electrolyte–active material composites such as Li_6PS_5Cl–$LiNi_{0.6}Co_{0.2}Mn_{0.2}O_2$,[17] Li_3PS_4–$LiNi_{0.6}Co_{0.2}Mn_{0.2}O_2$ [22] and Li_6PS_5Cl–Graphite.[20] In this work, two experimental approaches are taken: chronoamperometry (CA or direct-current (DC) polarization) and electrochemical impedance spectroscopy (EIS).

The electronic conductivities σ_e of composites in the compositional range Φ_{CAM} = 0.32 to 1.00, with Φ_{CAM} denoting the volume fraction of cathode active material (Li_2FeS_2) in $Li_{5.5}PS_{4.5}Cl_{1.5}$–Li_2FeS_2 composites, were determined by chronoamperometry. To do so, the samples were placed between stainless steel current collectors creating ion-blocking conditions to exclusively measure the electronic current response to the applied voltages. The resulting electronic currents follow the applied voltages linearly in agreement with Ohms law as exemplarily shown for Φ_{CAM} = 0.51 (Fig. 3a, blue markers and axis). With that, σ_e can be determined from the electronic resistance, $R_e \propto$ slope, and the geometrical information of the sample. An analogous experiment under different boundary conditions can be conducted to determine the ionic conductivity σ_{ion} of the composites. For this, SE and In/LiIn layers are symmetrically applied to both sides of the sample creating ion conducting, electron blocking conditions. With that, the resulting current response can be related exclu-

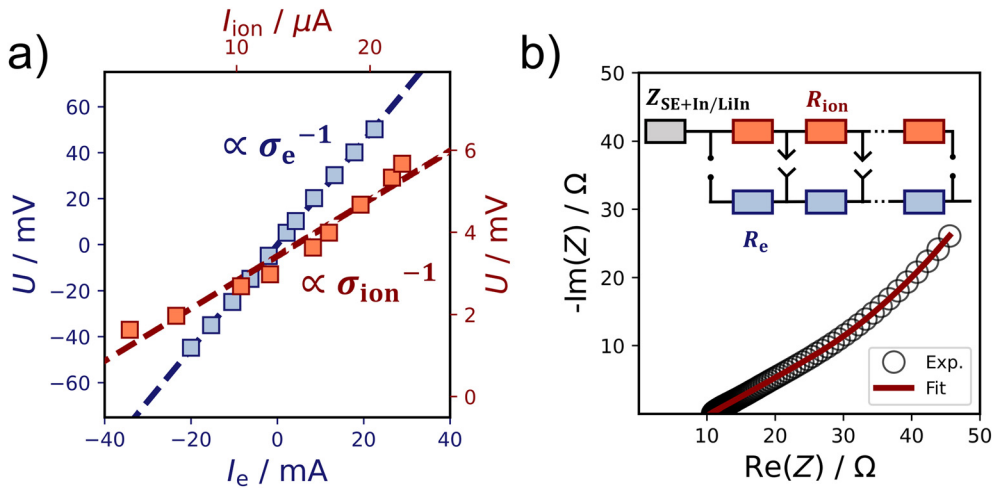

Fig. 3 (a) The results of chronoamperometry (CA) experiments in ion-blocking (blue markers and axis) and electron-blocking (red markers and axis) configuration. The effective electronic and ionic conductivities are inversely proportional to the slope of the depicted linear fit. (b) Impedance spectra of a half-cell at OCV after relaxation and before cycling of the cell. The data are described by the transmission-line model equivalent circuit depicted in the inset. $Z_{SE+In/LiIn}$ describes the impedance contributions of the reference electrode and separator, R_{ion} and R_e describe the ionic and electronic resistance of the cathode.

sively to the transport by ions. The ionic currents again follow Ohm's law (Fig. 3a, red markers and axis) allowing the determination of the ionic resistance R_{ion} and after subtraction of the electrode contributions, the ionic conductivity of the composites. These experiments reveal a significantly lower ionic conductivity compared to the electronic conductivity throughout the entire compositional range. While exemplarily shown for Φ_{CAM} = 0.51, all chronoamperometry results can be found in the ESI (Fig. S2–5†).

To corroborate the results of the chronoamperometry experiments, the effective ionic conductivity was determined from electrochemical impedance spectroscopy of half-cells in the configuration In/LiIn|$Li_{5.5}PS_{4.5}Cl_{1.5}$|Li_2FeS_2/$Li_{5.5}PS_{4.5}Cl_{1.5}$. A Z-type transmission line model[31,32] was used to fit the experimental results that describes ionic contact of the composite in direction of the separator and In/LiIn reference anode, and electronic contact in direction of the current collector (exemplarily shown for Φ_{CAM} = 0.51, Fig. 3b). The equivalent circuit shown as inset in Fig. 3b consists of an impedance $Z_{SE+In/LiIn}$ describing separator (R_{SE}) and interface contributions of the electrodes (parallel $R_{In/LiIn}$ and constant phase element with $C_{In/LiIn}$) as well as infinitely expanding branches of ionic and electronic resistances (R_{ion} and R_e) describing transport through the composite. During the fitting procedure R_e was fixed to the value approximated from chronoamperometry. With that, the applied equivalent circuit leads to a good description of the half-cell impedance response throughout the entire compositional range allowing the determination of the composite ionic conductivities. Again, all spectra and fits are shown in the ESI (Fig. S6†).

All conductivities are shown in Fig. 4a as a function of the CAM volume fraction. In the case of σ_{ion}, the average and standard deviations from both deployed techniques are depicted. The effective conductivities change exponentially as a function of the volume fraction of the active material. The ionic conductivity increases from $\sigma_{ion,CAM} = 5.4 \pm 0.3 \times 10^{-4}$ mS cm^{-1} to $\sigma_{ion,SE} = 6.1 \pm 0.2$ mS cm^{-1} between the pure phases, while the electronic conductivity decreases between $\sigma_{e,CAM} = 100 \pm 1$ mS cm^{-1} and $\sigma_{e,SE} = 10^{-6}$ mS cm^{-1},[33] respectively. This is the expected trend for the partial conductivities in composites considering effective medium theory.[34,35]

Effective medium theory describes the changes to the effective transport parameter in a composite as a function of the volume fraction of its constituents.[34,36,37] Multiple variations of effective medium theories exist and the reader is referred to the works by McLachlan and coworkers[36,37] for an overview. Here, we use the model derived by Wu and coworkers[35] that is closely related to the general Bruggeman[34,38] equation to describe the observed trends in the effective conductivities. The model describes the relation between the effective conductivity of the composite and the conductivity of its constituents following:[35]

$$\frac{\sigma_{eff} - \sigma_1}{k \cdot \sigma_{eff} + \sigma_1}\phi_1 + \frac{\sigma_{eff} - \sigma_2}{k \cdot \sigma_{eff} + \sigma_2}\phi_2 = 0, \quad (5)$$

where σ_{eff} is the effective conductivity of the composite and $\sigma_{1,2}$ and $\Phi_{1,2}$ are the conductivities and volume fractions of phase 1 and 2, respectively. Porosity is not specifically considered as third phase in this study, the effect of which is expected to be negligible given constant degrees of porosity between all composites in first approximation. The parameter k is a constant that describes the connectivity of the phases within the composite and determines the percolation threshold. Subsequently, the data have been fit by solving eqn (5) for σ_{eff} and using k and the conductivity of the better conducting phase ($\sigma_{e,CAM}$ for σ_e and $\sigma_{ion,SE}$ for σ_{ion}) as fitting para-

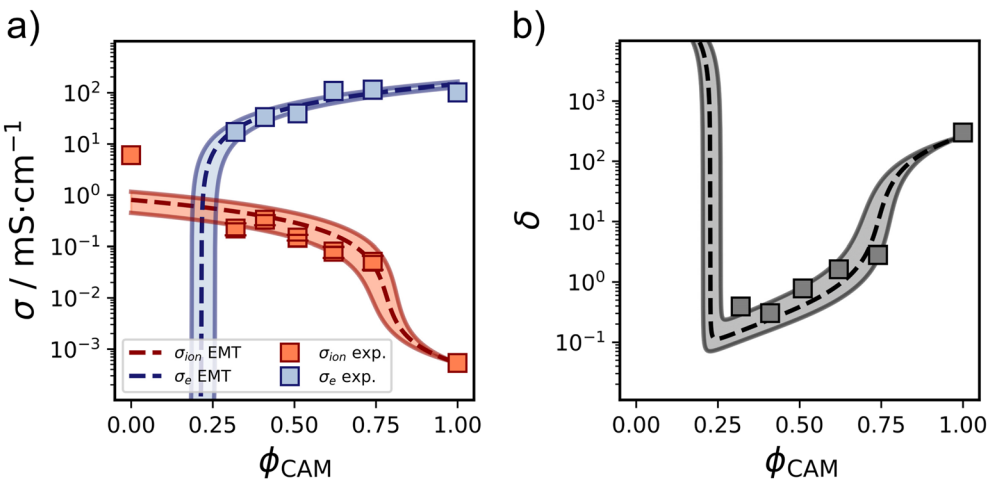

Fig. 4 (a) Effective ionic and electronic conductivities as a function of the active material volume fraction. The experimentally determined electronic (CA) and ionic (from CA and EIS) conductivities are shown as a function of the CAM volume fraction. Dashed lines correspond to the effective medium theory (EMT) fit to the data while bold lines and shaded areas depict the uncertainty area of the fit. (b) Dimensionless current density δ calculated considering current densities corresponding to 0.134C, thicknesses corresponding to a mass loading of 15.3 mg cm^{-2} and the experimental and effective-medium modeled conductivities depicted in (a). The δ-parameter shows a minimum at low Φ_{CAM} where the electrode transport is closest to fulfilling the condition $\sigma_{ion} \approx \sigma_e$.

meters. With that, the experimental results of both conductivities can be well described (dashed lines in Fig. 4a) allowing to approximate the effective transport between and closely surrounding the investigated compositional space of the cathode. The final fitting equation $\sigma_{eff}(\sigma_1, \sigma_2, \Phi_1, \Phi_2, k)$, the resulting fitting parameters and details of the procedure are given in the ESI.† Importantly, the effective medium model does not account for any interfacial effects between both phases, or grain boundary transport/resistance that can explain deviations between fit and data.

In the next step, to understand potential transport limitations in the cathodes, the model by Newman and Tobias for porous electrodes is taken into consideration.[23] Specifically, we evaluate if the dimensionless current density δ (eqn (4)) can guide our understanding of transport related differences in cathode performance as a qualitative descriptor. Again, δ is a function of the effective conductivities, the cathode thickness and the applied current density and introduced as a descriptor for the tendency of the cathode to show nonuniform reaction rate distributions ($\delta \gg 1$), the buildup of reaction fronts and state-of-charge gradients.[19,30] It must be considered that this descriptor, without accounting for important microstructural features like CAM-SE contact area, and kinetic parameters such as exchange current densities, can only be evaluated as qualitative, and not quantitative descriptor to predict potential transport limitations in the cathode. Nonetheless, we expect these transport limitations to scale with transport-related performance properties of the cathode, *e.g.*, the cathode utilization (general contacting of CAM and SE) and rate capability and these trends are reported in literature, where cathode utilization decreases because either σ_{ion} or σ_e are insufficiently high or when the cathode thickness and applied current density are increased.[17,18,20,22]

The δ-parameters characterizing the investigated Li_2FeS_2–$Li_{5.5}PS_{4.5}Cl_{1.5}$ cathodes are shown in Fig. 4b. The depicted values are calculated according to eqn (4) using the experimental (markers) and effective medium modelled effective conductivities (dashed line and shaded area) as input parameter. Moreover, the thicknesses L and current densities i of the cathodes later investigated as a function of the CAM volume fraction are utilized for the calculation. These are in the range of 85 μm to 73 μm, and 0.24 mA cm^{-2} to 0.49 mA cm^{-2} (0.134C) for Φ_{CAM} between 0.32 and 0.74 at constant cathode mass, respectively. An overview of the parameters is given in Table S3 of the ESI.†

The experimental δ-parameters express a minimum of 0.3 at Φ_{CAM} = 0.41, with a steady increase to 2.8 at Φ_{CAM} = 0.74. These values are close to or below the empirical condition of $\delta \lesssim 1$ for which a uniform distribution of reaction rates is expected.[23,27] Considering σ_{ion} and σ_e from effective medium theory, the minimum of δ occurs at even lower Φ_{CAM} just before the percolation threshold of electronic conduction is reached. For fractions of $\Phi_{CAM} > 0.74$, δ increases significantly as a consequence of reaching the percolation threshold of σ_{ion}. With that, for pure Li_2FeS_2, a value of 300 is obtained indicating the onset of strong transport limitations ($\delta \gg 1$). Following, cathodes relating to these δ-parameters are investigated in terms of electrochemical performance and the potential of δ as a qualitative descriptor is evaluated.

Performance of the cathode composites

The electrochemical performance of the cathodes with varying fraction of CAM have been investigated in half cells using a In/LiIn counter electrode and $Li_{5.5}PS_{4.5}Cl_{1.5}$ as separator. Initially, cells with constant cathode composite mass loading (15.3 mg cm^{-2}) are characterized to evaluate the influence of Φ_{CAM} on the performance at comparable cathode thicknesses. These are, approximated by the relative density of the cathode and its mass, in the range of 73 μm to 85 μm (Table S3†). All composites were first cycled at a constant C-rate of 0.134C assuming a theoretical specific capacity of 300 mA h g^{-1} (corresponding to 0.1C assuming a theoretical capacity of 400 mA h g^{-1} for full delithiation). Afterwards, rate capability was tested at constant current densities instead. An overview of all 0.134C rates in terms of current densities, and all current densities in terms of C-rates, is given in Table S3 of the ESI.† In addition, scanning electron micrographs and energy dispersive X-ray spectroscopy signals are shown in Fig. S8† characterizing the composite microstructures.

The voltage profiles of the solid-state cathodes do not significantly change as a function of the cathode composition. A comparison of the profiles at the first cycle is given in Fig. 5a. The charge profile is characterized by a monotonically increase of the voltage with weakly pronounced features below 1.9 V. In this regime, delithiation is charge balanced by oxidation of Fe^{2+} to Fe^{3+} corresponding to the nominal compositional range of Li_2FeS_2 to $Li_{1.5}FeS_2$ and the profiles of the solid-state cathodes agree well with reports using liquid electrolyte (dashed line in Fig. 5a).[10] At 1.9 V, a voltage plateau representing the two-phase regime of $Li_{1.5}FeS_2$–$Li_{0.5}FeS_2$ establishes. This region can contribute a theoretical capacity of 200 mA h g^{-1}. This is the case in liquid electrolyte based cells,[10] while the plateau is generally lower capacity in the investigated solid-state cathodes (Fig. 5a).

Furthermore, solid-state cells show significantly lower Coulomb efficiencies in the first cycle with values between 77% and 82% in the solid-state, compared to ≈90% in the liquid electrolyte based cells.[10] Low first cycle efficiencies are common in other solid-state battery chemistries, *e.g.*, using Li(Ni,Co,Mn)O_2 as active material and generally, they are related to contact losses between the active material and the SE due to volumetric expansion as well as the formation of a SE-CAM interphase (CEI).[39,40] The capacity retentions reflect the low initial efficiency in the first cycle, with gradual capacity losses afterwards (Fig. 5b). The capacity retentions are comparable in general, but cathodes with the highest Φ_{CAM} show a lower overall capacity retention of 73% (average Coulomb efficiency of 98.3%) compared to 85% (average Coulomb efficiency of 99.5%) for cathodes with the lowest Φ_{CAM} after 40 cycles. Given the special role of the first charge cycle, these relative retentions and average efficiencies are referring to or count from the second charge onward. In addition to the capacity reten-

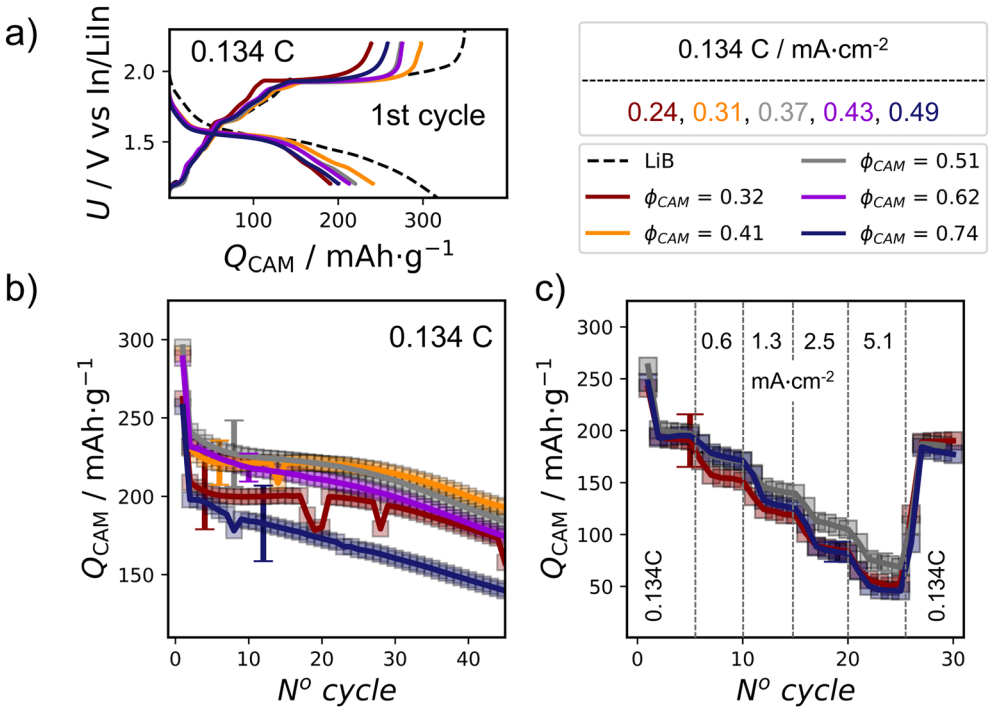

Fig. 5 The legend in the top right defines datasets in all subplots. Additionally, a conversion from the 0.134C rates to the applied current densities for cells with varying CAM volume fraction Φ_{CAM} is given color coded in the top right. (a) Voltage profiles of cells employing $Li_{5.5}PS_{4.5}Cl_{1.5}$–Li_2FeS_2 cathodes of varying CAM volume fraction Φ_{CAM} during the first cycle under a rate of 0.134C. The profile of the first cycle is compared to Li_2FeS_2 cathodes using liquid electrolyte[10] (dashed line). (b) Capacity retention at a constant rate of 0.134C and (c) upon increasing the applied current density tested for composites with three compositions (see inset). Standard deviations from triplicates for each dataset are given at an arbitrary representative cycle.

tion with ongoing cycling, the rate capability was tested for exemplary compositions of Φ_{CAM} = 0.32, 0.51 and 0.74 (Fig. 5c). In agreement with the constant C-rate cycling, no strong compositional trends can be observed in the rate retention upon first visual inspection of the data.

Based on this first assessment, we now discuss the performance as a function of the cathode configuration in detail. Thereby, focus lies on performance parameters that are related to the effective transport properties of the cathode discussed beforehand (Fig. 4), the initial cathode utilization and the rate performance.

Initial cathode utilization and areal capacity

The initial cathode utilization is related to the transport given that it is a measure of the contacted and electrochemical active CAM in the composite, *i.e.*, how accessible and at which rate active material particles are for both charge carriers. In the following, the initial cathode utilization is measured by the average capacity per gram CAM Q_{CAM}. The average includes both, the average over the first five cycles (excluding first charge) of each individual cell, and the average and standard deviation of all cells investigated with the same composition.

The comparison of Q_{CAM} as a function of Φ_{CAM} acquired at a rate of 0.134C shows no strong changes of the cathode utilization, with a maximum difference of 15% between the highest capacity of Q_{CAM} = 229 ± 28 mA h g^{-1} at Φ_{CAM} = 0.62 and the lowest of 195 ± 10 mA h g^{-1} at Φ_{CAM} = 0.74 (Fig. 6a, left). Given the absence of a strong loss of capacity utilization, and to explore limitations of the cell chemistry, the areal loading is further increased by testing the extreme of a pure Li_2FeS_2 cathode (Φ_{CAM} = 1.0) and by increasing the cathode thickness from 73 μm to 110 μm and 145 μm for a cathode with Φ_{CAM} = 0.74. A drastic decrease of the cathode utilization occurs going to Φ_{CAM} = 1.0, with a decrease by 90% to capacities of 25 ± 3 mA h g^{-1}. At the same time, increasing the thickness of the composite only leads to a Q_{CAM} decrease from 195 ± 10 mA h g^{-1} to 181 ± 14 mA h g^{-1} (7% decrease).

Porous electrode theory can guide the understanding of these trends given that it aims to describes the reaction rate distribution throughout the cathode, as quantified by the δ-parameter (eqn (4) and Fig. 2). With that, the δ-parameter (eqn (4) and Fig. 4b) should be capable of capturing qualitative trends in cathode utilization. The capacities of all cells as a function of δ are depicted in the right subplot of Fig. 6a. As a reminder, δ not only considers changes to the effective conductivities by changing Φ_{CAM}, but variations in the applied current density, a consequence of using constant C-rates, and the cathode thickness. Moreover, no strong changes to the cathode utilization should occur for cathodes characterized by values of $\delta \lesssim 1$ that describes the condition of uniform reaction rate distributions.

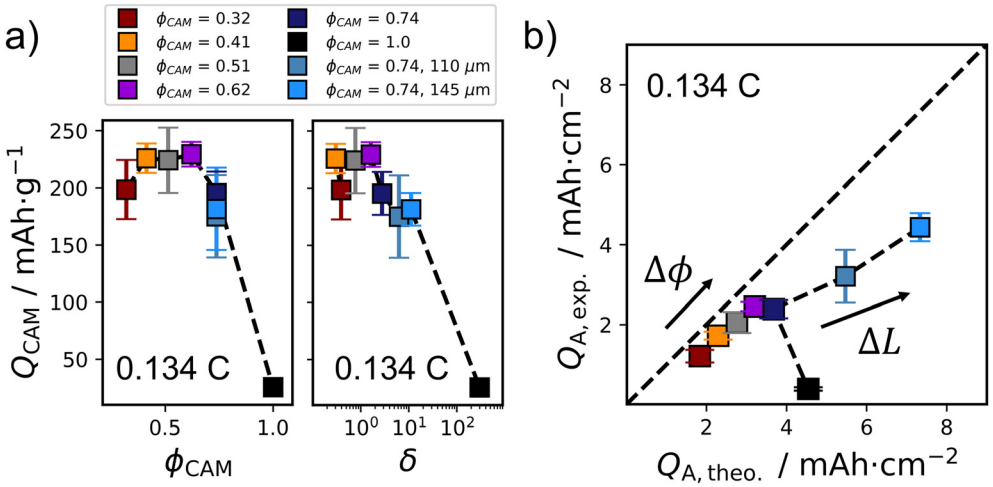

Fig. 6 (a) Initial charge capacity per mass CAM (Q_{CAM}) as a function of (left) the CAM volume fraction and (right) the δ-parameter (eqn (6)). Uncertainties correspond to the standard deviation of at least three cells per composition. (b) The corresponding experimentally achieved areal capacities as a function of the areal loading for the cells depicted in (a). The gray-dashed line gives a reference for full cathode utilization. $\Delta\Phi$ and ΔL highlight trends with increasing CAM volume fraction and cathode thickness.

This is the case for all composites in the range of Φ_{CAM} = 0.32 to 0.74 at 0.134C and with thicknesses between 85 μm and 73 μm (Fig. 6a, right). For these cells, the δ-parameter ranges between 0.3 and 2.8 (Fig. 4b). Consequently, the δ-parameter analysis predicts high uniformity of the reaction rate distribution and gives a rational for the marginal changes in cathode utilization. Increasing the cathode thickness and, considering constant C-rates, the applied current density, increases the value of δ from 2.8 to 6.3 and 11.1, moving away from the desired condition of $\delta \lesssim 1$ and explaining the decrease of the cathode utilization going to a thick electrode configuration. For the edge case of pure Li_2FeS_2 as cathode, the δ-parameter significantly increases to ≈300 driven by the orders of magnitude loss in effective ionic conductivity (Fig. 4). This strong increase manifests as a 90% decrease of the cathode utilization. With that, the δ-parameter captures the observed trends in the initially achieved capacities qualitatively. Moreover, a decrease of Q_{CAM} with the logarithm of δ can be observed, acknowledging the scattering in the dataset (Fig. 6a). Not considered in this analysis is the residual porosity of the electrodes. Nonetheless, given that the relative density does not change significantly with an average of 85 ± 3% for all investigated electrodes, the effect is assumed to be negligible in first approximation.

This qualitative trend agrees with literature results considering the δ-parameters approximated from reported values of σ, i and L. Systems that indicate first signs of transport limitations and underutilization of the electrode are characterized by values of ≈19 ($LiNi_{0.6}Co_{0.2}Mn_{0.2}O_2$–$Li_3PS_4$),[22] ≈ 22 ($LiCoO_2$–$Li_{10}GeP_2S_{12}$)[18] and ≈31 (Graphite–$Li_6PS_5Cl$).[20] Moreover, Bradbury and coworkers[19] showed that severe reaction fronts occur in Li–S cells that are characterized by a δ-parameter of ≈200 agreeing with the significant utilization loss when going to pure Li_2FeS_2 ($\delta \approx 300$).

The relatively small variations in Q_{CAM} by 15% between all Φ_{CAM} of comparable thickness, and by 7% when doubling the cathode thickness at constant composition, rationalized by the δ-parameter analysis, are promising outlooks for the Li_2FeS_2 battery chemistry. While these are significant changes to the cathode utilization, the loss in utilization is marginal compared to the areal loading increase from 1.8 mA h cm^{-2} to 3.7 mA h cm^{-2} with increasing Φ_{CAM}, and to 7.3 mA h cm^{-2} upon increasing the cathode thickness. This increase of the areal loading by a factor of approximately five compensates the at maximum 22% loss in cathode utilization, so that the achieved areal capacities increase from 1.2 mA h cm^{-2} to 4.4 mA h cm^{-2} going from the lowest to the highest areal loadings (Fig. 6b). Clearly, the higher δ – for instance in thicker electrodes – the more deviations of the attained capacity to the theoretical capacity can be expected.

Rate capability

The analysis of the initial cathode utilizations and areal capacities shows that $Li_{5.5}PS_{4.5}Cl_{1.5}$–Li_2FeS_2 cathodes with high volume fractions of CAM can be realized successfully. Moreover, the achievable areal capacities can be increased further with the thickness of the cathode. Nonetheless, fast charging is desired for application and the rate capability of the electrodes needs to be considered. Therefore, electrodes with Φ_{CAM} = 0.32, 0.51 and 0.74 ($L \approx 80$ μm), and with L = 73, 110 and 145 μm (for Φ_{CAM} = 0.74) have been tested for five cycles per current density step, starting with a current density corresponding to the theoretical rate of 0.134C (respective current densities listed in Table S3†). Subsequently, the applied current density was stepwise changed between 0.6 mA cm^{-2} and 5.1 mA cm^{-2}. This routine was chosen to compare the composites at constant current densities despite changes to the cathode loading and with that the C-rates. The average

capacity Q_{CAM} of the five charge cycles per current density step, and the average of triplicates as well as their standard deviation, are considered in the following discussion. The rate retention as a function of the applied current density is shown in the ESI (Fig. S12†). Here, we rescale the applied current density to a practical rate of charge denoted r as proposed by Tian and coworkers.[41] The practical rate in units of h^{-1} is defined, following:[41]

$$r = I/Q_{exp}(I), \quad (6)$$

where I is the applied current (in mA) and $Q_{exp}(I)$ (in units of mA h) is the experimentally achieved capacity at that current. Thereby, this definition of rate differs from the definition of the C-rate by relating the current to a practical rather than a theoretical capacity. With that, the inverse of the practical rate directly represents the time in which the charge was acquired.[41]

The cathode utilizations as a function of the practical rate are shown in Fig. 7a. At the highest applied current density, cathodes with Φ_{CAM} = 0.32 and 0.74 and comparable thickness achieve similar capacities of 55 mA h g^{-1} and 51 mA h g^{-1}, respectively. Nonetheless, this capacity is achieved at a significantly higher practical rate of 14.9 h^{-1} (3.1C) for Φ_{CAM} = 0.32 compared to 8.2 h^{-1} (1.6C) for Φ_{CAM} = 0.74 showing better rate performance of cathodes with lower CAM fractions. Increasing the thickness from 73 μm to 145 μm for the composition Φ_{CAM} = 0.74 leads to further lowering of the rate capability. Again, considering the highest applied current, the capacity per CAM mass is lowered to 44 mA h g^{-1} and acquired at an even lower rate of 4.8 h^{-1} (0.8C). This indicates a systematic decrease of rate capability when increasing the areal loading of the cathode, *e.g.*, by increasing Φ_{CAM} or its thickness.

To test this hypothesis, we use the semi-empirical model proposed by Tian and coworkers[41] to quantify the rate behavior. The model relates the capacity, or cathode utilization $Q_{CAM}(r)$, to the practical rate r, following:[41]

$$Q_{CAM}(r) = Q_{CAM,0}[1 - (r\tau)^n(1 - e^{-(r\tau)^{-n}})], \quad (7)$$

where $Q_{CAM,0}$ is the capacity achieved at the lowest rate and τ and n are parameters to describe the data. While τ and n are related to physical properties of the system by the authors,[41] they are solely utilized to quantify the rate capability in this work. In general, τ (in units of h) is inversely proportional to the turning point in rate at which accelerated capacity fading sets on and n describes the slope of the accelerated capacity fading with rate (see insets in Fig. 7a). Thereby, low values of τ and n describe good rate capability, *i.e.*, the onset of accelerated fading occurs at higher rates for low values of τ, and the accelerated fading is less pronounced for low values of n.[41]

Applying this model, eqn (7) describes the rate performance of the investigated cathodes (dashed lines in Fig. 7a). Moreover, the resulting parameters τ and n confirm the initial hypothesis from visual inspection with both showing a detrimental linear increase with the areal loading of the cathode (Fig. 7b). To understand this observation, we again consider the δ-parameter introduced in the porous electrode theory. While at a rate of 0.134C, the δ-parameter was close to unity for most of the investigated cathodes, indicating uniform reaction rates and explaining the good cathode utilization even at high CAM volume fractions (Fig. 6a), the average δ-parameter over the investigated current density range δ_{avg} is significantly increased. At a composition of Φ_{CAM} = 0.32 this translates to δ_{avg} = 3, while for the highest CAM volume fraction and thickness this value is increased to δ_{avg} = 22. This significant increase of δ_{avg} with increase of Φ_{CAM} and the cathode thickness indicates that nonuniformity of the reaction rate distribution, measured by δ_{avg}, can occur as consequence of applying higher current densities. In fact, the parameters τ and n

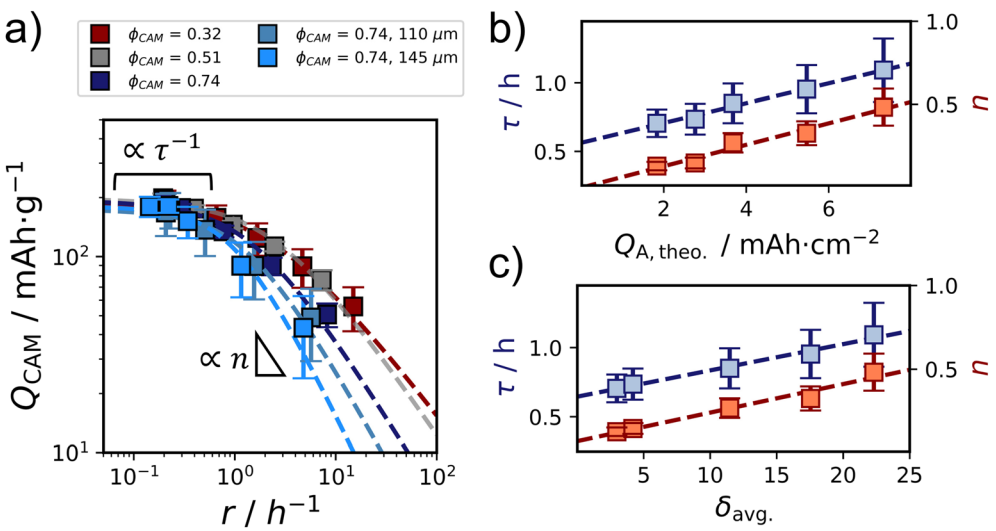

Fig. 7 (a) Capacity retention of cells with varying cathode composition and thickness as a function of the practical rate r as defined in the main text. Dashed lines correspond to fits to the data using the semi-empirical analytical model proposed by Tian *et al.*[41] (b) The parameters τ (blue) and n (red) obtained from fitting the data shown against the areal loading of the cells and (c) the average δ over the investigated current density range.

quantifying the rate capability increase linearly as a function of δ_{avg} (Fig. 7c) corroborating this hypothesis.

With that, it can be assumed that the decrease of rate performance with areal loading (Fig. 7b) can at least be partly explained by the onset of reaction rate nonuniformities at higher rates (Fig. 7c). Nonetheless, it must be noted that Q_{CAM} cannot be unambiguously related to δ. An overview of all $Q_{CAM}(\Phi_{CAM}, L, i)$ as a function of $\delta(\Phi_{CAM}, L, i)$ is shown in the ESI (Fig. S13†). Other factors such as poor ionic contacting of the CAM at high Φ_{CAM} and the increased likelihood of isolated CAM regions in thick electrode configuration can contribute to the decreased cathode utilization and rate performance additionally and are not captured by the δ-parameter analysis.

Energy density and transport balancing of the cathode

After examination of the initial capacity retention (Fig. 6) and the rate capability (Fig. 7), cathode composites are now evaluated regarding their (rate dependent) gravimetric energy density. In agreement with the discussion of the rate capability, the energy density is calculated from the average capacities of five cycles at a certain current density step, and the average and standard deviation of triplicates (with that relating to the data depicted Fig. 7a). Furthermore, only the mass of the cathode, the In/LiIn and the separator are considered for calculation of the gravimetric energy density. The latter two are constant for all investigated cathodes.

Comparing the gravimetric energy densities for cells with Φ_{CAM} = 0.32, 0.51 and 0.74 as a function of the practical rate (eqn (6)), it becomes evident that the gravimetric energy density can be significantly increased from 11.4 to 41.4 W h kg^{-1} by increasing Φ_{CAM} and the cathode thickness L (Fig. 8a) at low rates. This is, because the areal loading of the cathode is increased from 1.8 to 7.3 mA h cm^{-2}, while the simultaneous cathode utilization decrease is negligible in comparison in agreement with the δ-parameter analysis (Fig. 6b). Nonetheless, this strong energy density increase is relativized going to higher rates, *i.e.*, higher applied current densities (overview in Table S3†). At higher rates, and with that upon increasing δ significantly, the energy densities of all investigated cells start to converge to ≈5 W h kg^{-1} given the systematic decrease of the rate capability (Fig. 7) when increasing the areal loading of the cathode.

This highlights that high energy densities can be practically achieved at low rates, but $Li_2FeS_2/Li_{5.5}PS_{4.5}Cl_{1.5}$ solid-state cathodes require further improvement regarding their rate capability. This can be achieved, *e.g.*, by improving the processing of the solid composites and by controlling the particle size distribution of its constituents. Both strategies have the ability to improve the transport properties[42,43] of cathodes at a constant Φ_{CAM} and with that are suitable attempts to increase the rate performance for cathodes with high areal loading. Nonetheless, Li_2FeS_2 solid-state electrodes show overall promising performances, especially given the vast design space that has yet to be explored for this novel CAM, *e.g.*, the use of coatings to increase the longevity, or further processing to control crystallinity in addition to the particle sizes.

The comparison of achievable energy densities further highlights the importance of evaluating cell chemistries at realistic, application-relevant areal loadings, *i.e.*, high CAM volume fractions, in thick electrode configuration and at high applied current densities, given the strong influence on electrode utilization. These trends, often intuitive for battery scientists, can be understood qualitatively by considering the δ-parameter introduced by Newman and Tobias.[23]

With that, a widespread analysis of electrodes considering this descriptor can guide electrode design and detect or

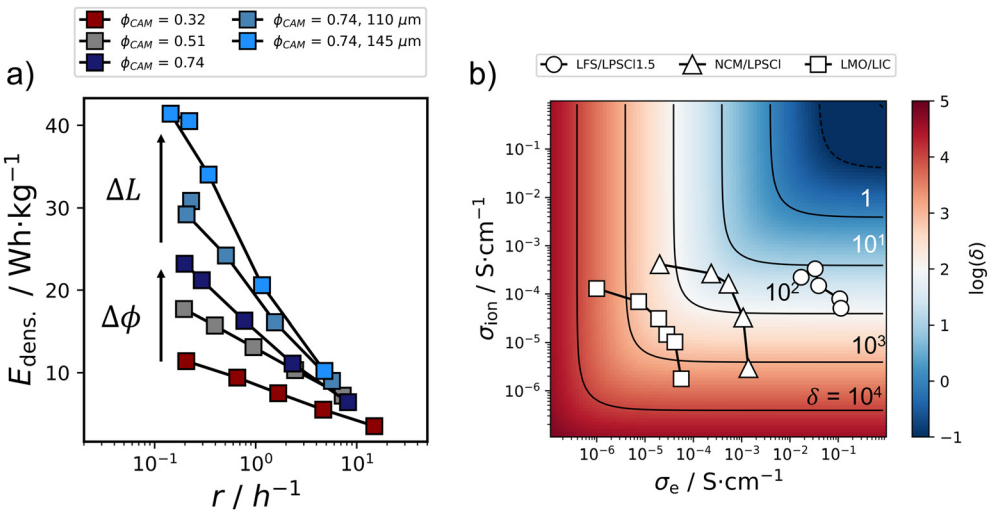

Fig. 8 (a) Gravimetric energy density as a function of the practical rate (eqn (6)). $\Delta\Phi_{CAM}$ and ΔL highlight trends with increasing CAM volume fraction and cathode thickness. (b) Partial ionic and electronic conductivity of different electrode composites with varying CAM volume fraction in context of the δ-parameter (eqn (4), L = 200 µm, i = 5 mA cm^{-2}). The depicted data correspond to Li_2FeS_2 (LFS)/$Li_{5.5}PS_{4.5}Cl_{1.5}$ (LPSCl1.5, this work), $LiNi_{0.6}Co_{0.2}Mn_{0.2}O_2$ (NCM)/Li_6PS_5Cl (LPSCl, Minnmann *et al.*[17]) and $LiMn_2O_4$ (LMO)/Li_3InCl_6 (LIC, Hendriks *et al.*[44]). The δ-parameter scale is calculated for a two-electron reaction (n_e = 2 in eqn (4)) with that slightly overestimating the expected values for NCM and LMO.

predict potential problems heading to application, even in the early stages of research and development. Considering the transport of different active material/electrolyte systems, *e.g.*, $Li_2FeS_2/Li_{5.5}PS_{4.5}Cl_{1.5}$ (this work), $LiNi_{0.6}Co_{0.2}Mn_{0.2}O_2/Li_6PS_5Cl$ (Minnmann *et al.*[17]) and $LiMn_2O_4/Li_3InCl_6$ (Hendriks *et al.*[44]), on this unified δ-parameter scale, allows their direct comparison from a transport perspective (Fig. 8b). At a thickness of 200 μm and an applied current density of 5 mA cm^{-2}, the most transport-optimized $LiNi_{0.6}Co_{0.2}Mn_{0.2}O_2$- (triangles) and Li_2FeS_2-based (circles) electrodes are characterized by $\delta \approx 30$ ($LiNi_{0.6}Co_{0.2}Mn_{0.2}O_2$) and ≈11 ($Li_2FeS_2$) and with that are expected to still show reasonable performance. This is supported by the results in this work, where cathodes with low CAM volume fraction show the best rate performance (Fig. 7a), and in agreement with the reported rate performances by Minnmann and coworkers.[17] In both cases, this optimum in rate performance is achieved in cathode compositions closest to the condition of $\sigma_e \approx \sigma_{ion}$ (diagonal in Fig. 8b) that minimizes the conductivity term of the δ-parameter (eqn (4) and Fig. 2b). Moreover, this analysis shows that the investigated system is strongly limited by σ_{ion} and that increasing the cell performance is intimately tied to the improvement of the ionic conductivity in the composite (to reach the condition of $\sigma_e \approx \sigma_{ion}$). The highest electrode utilization in the system $LiMn_2O_4/Li_3InCl_6$ [44] is also reported at the composition fulfilling the condition $\sigma_e \approx \sigma_{ion}$ in agreement with the δ-parameter assessment. Nonetheless, the analysis predicts that the system should suffer from transport limitations in thick electrode configurations and during fast charging ($\delta \approx 160$) even at the optimized composition given the lower order of magnitude in both conductivities.

In general, this assessment shows that solid-state cathode composites are limited by their ionic conductivity that is <1 mS cm^{-1}, while the electronic conductivity between active materials spreads a wide range and can be optimized more freely by introducing electron conducting additives. Consequently, the search for faster ion conducting solid electrolytes, and the improvement of the solid electrolyte percolation in the electrode, are of highest importance for the development of solid-state batteries in outlook on application. This need for higher conducting solid electrolyte is further emphasized by the exponential loss[17,44] in ionic conductivity (Fig. 4a) when increasing the CAM volume fraction in the cathode that is necessary to enable high areal loadings. This additionally shows that good ionically conducting active materials should be explored, as they promise a softening of the loss in effective (ionic) conductivity when going to high volume fractions of active species.

Lastly, it has to be noted that while the δ-parameter gives an intuitive way of comparing chemistries regarding their electrode utilization, and potential challenges in rate retention, it does not include information about other important metrics such as cycle stability. In addition, the transport discussion in this study is based exclusively on as-prepared cathodes, but state-of-charge dependent conductivities should be considered to provide a full understanding of transport-related effects on performance, if available.

Conclusion

In conclusion, this work highlights the importance of balanced transport in composite cathodes and shows that the "transport quality" of the electrode can be qualitatively captured by the δ-parameter derived in porous electrode theory. With that, it is shown that transport is sufficiently balanced in $Li_2FeS_2/Li_{5.5}PS_{4.5}Cl_{1.5}$ cathodes, allowing cathode configurations with high areal loadings of 7.3 mA h cm^{-2} to perform well at low rates with initial capacities of 4.4 mA h cm^{-2}. Nonetheless, increasing the areal loading by deviating from optimal transport balancing subsequently leads to a worsening of the rate performance, as both, the increased cathode thickness (73 to 145 μm) and current densities (0.6 to 5.1 mA cm^{-2}) amplify existing transport limitations. These trends can be understood considering the δ-parameter. Moreover, the δ-parameter has the potential to unify the assessment of electrode quality and potential of different cell chemistries. For example, introducing an arbitrary cut-off in δ, the maximum CAM volume fraction, thickness (areal loading), and applied current densities, achievable before reaching this condition, can be evaluated. Porous electrode theory proposes the absence of transport limitations for $\delta \lesssim 1$ and the onset of significant cathode utilization losses are observed in the range $1 \leq \delta \leq 10$ in this work, with higher sensitivity for changes in current density than electrode thickness and CAM volume fraction.

The loss in rate capability with increased areal loading motivates studies that focus on processing optimization and particle size matching as strategies to improve transport in cathodes with high areal loading. This is because improving the partial ionic conductivity will lower the δ-parameter independent on electrode thickness and applied current density. Moreover, this work highlights the importance of investigating electrodes with realistic energy densities already on the lab-scale. Thereby, the potential of new cell chemistries in outlook to application can be evaluated from the start and problems can be targeted before upscaling of the technology is attempted.

Author contributions

The manuscript was written through contributions of all authors. All authors have given approval to the final version of the manuscript. T. B.: conceptualization, experimental investigation, formal analysis, data curation, writing, visualization. L. K.: data evaluation, experimental investigation, writing-review and editing. B. H.: experimental investigation, writing-review and editing. M. A. K.: conceptualization, methodology, writing-review and editing. K. A. S.: experimental investigation, writing-editing and review. W. G. Z.: conceptualization, resources, writing-review and editing, supervision.

Data availability

The data that support the findings of this study have been archived at **https://doi.org/10.17879/45968568801**.

Conflicts of interest

There are no conflicts to declare.

Acknowledgements

The authors acknowledge financial support by the Bundesministerium für Bildung und Forschung (BMBF; projects KAROFEST 03XP0498B). We further acknowledge funding from the Deutsche Forschungsgemeinschaft under project number 459785385. The authors acknowledge the help of Andrew J. Martinolich in the early stages of this study.

References

1 J. Janek and W. G. Zeier, *Nat. Energy*, 2016, **1**, 1–4.
2 J. Janek and W. G. Zeier, *Nat. Energy*, 2023, **8**, 230–240.
3 S. Randau, D. A. Weber, O. Kötz, R. Koerver, P. Braun, A. Weber, E. Ivers-Tiffée, T. Adermann, J. Kulisch, W. G. Zeier, F. H. Richter and J. Janek, *Nat. Energy*, 2020, **5**, 259–270.
4 H. C. Urey, *Phys. Rev.*, 1952, **88**, 248–252.
5 C. H. Jung, H. Shim, D. Eum and S. H. Hong, *J. Korean Ceram. Soc.*, 2021, **58**, 1–27.
6 G. Whang and W. G. Zeier, *ACS Energy Lett.*, 2023, **8**, 5264–5274.
7 W. J. Zhang, *J. Power Sources*, 2011, **196**, 2962–2970.
8 P. G. Bruce, S. A. Freunberger, L. J. Hardwick and J. M. Tarascon, *Nat. Mater.*, 2012, **11**, 19–29.
9 Y. Zhu, X. He and Y. Mo, *J. Mater. Chem. A*, 2016, **4**, 3253–3266.
10 C. J. Hansen, J. J. Zak, A. J. Martinolich, J. S. Ko, N. H. Bashian, F. Kaboudvand, A. Van Der Ven, B. C. Melot, J. Nelson Weker and K. A. See, *J. Am. Chem. Soc.*, 2020, **142**, 6737–6749.
11 J. Barker and E. Kendrick, *J. Power Sources*, 2011, **196**, 6960–6963.
12 A. J. Martinolich, J. J. Zak, D. N. Agyeman-Budu, S. S. Kim, N. H. Bashian, A. Irshad, S. R. Narayan, B. C. Melot, J. Nelson Weker and K. A. See, *Chem. Mater.*, 2021, **33**, 378–391.
13 L. Blandeau, G. Ouvrard, Y. Calage, R. Brec and J. Rouxel, *J. Phys. C: Solid State Phys.*, 1987, **20**, 4271–4281.
14 C. D. Wei, H. T. Xue, X. D. Zhao and F. L. Tang, *Phys. Chem. Chem. Phys.*, 2023, **25**, 8515–8523.
15 K. Takada, Y. Kitami, T. Inada, A. Kajiyama, M. Kouguchi, S. Kondo, M. Watanabe and M. Tabuchi, *J. Electrochem. Soc.*, 2001, **148**, A1085.
16 K. Takada, K. Iwamoto and S. Kondo, *Solid State Ionics*, 1999, **117**, 273–276.
17 P. Minnmann, L. Quillman, S. Burkhardt, F. H. Richter and J. Janek, *J. Electrochem. Soc.*, 2021, **168**, 040537.
18 Y. Kato, S. Shiotani, K. Morita, K. Suzuki, M. Hirayama and R. Kanno, *J. Phys. Chem. Lett.*, 2018, **9**, 607–613.
19 R. Bradbury, G. F. Dewald, M. A. Kraft, T. Arlt, N. Kardjilov, J. Janek, I. Manke, W. G. Zeier and S. Ohno, *Adv. Energy Mater.*, 2023, **13**, 2203426.
20 A. L. Davis, V. Goel, D. W. Liao, M. N. Main, E. Kazyak, J. Lee, K. Thornton and N. P. Dasgupta, *ACS Energy Lett.*, 2021, **6**, 2993–3003.
21 A. Bielefeld, D. A. Weber and J. Janek, *J. Phys. Chem. C*, 2019, **123**, 1626–1634.
22 K. G. Naik, B. S. Vishnugopi and P. P. Mukherjee, *ACS Appl. Mater. Interfaces*, 2022, **14**, 29754–29765.
23 J. S. Newman and C. W. Tobias, *J. Electrochem. Soc.*, 1962, **109**, 1183.
24 W. Zhang, D. A. Weber, H. Weigand, T. Arlt, I. Manke, D. Schröder, R. Koerver, T. Leichtweiss, P. Hartmann, W. G. Zeier and J. Janek, *ACS Appl. Mater. Interfaces*, 2017, **9**, 17835–17845.
25 K. Micka, *ACS Advances in Chemistry*, 1969, pp. 73–81.
26 J. Euler and W. Nonnenmacher, *Electrochim. Acta*, 1960, **2**, 268–286.
27 J. Newman and W. Tiedemann, *AIChE J.*, 1975, **21**, 25–41.
28 C. Wagner, *J. Electrochem. Soc.*, 1951, **98**, 116–128.
29 E. J. F. Dickinson and A. J. Wain, *J. Electroanal. Chem.*, 2020, **872**, 114145.
30 A. M. Stavola, X. Sun, D. P. Guida, A. M. Bruck, D. Cao, J. S. Okasinski, A. C. Chuang, H. Zhu and J. W. Gallaway, *ACS Energy Lett.*, 2023, **8**, 1273–1280.
31 Z. Siroma, N. Fujiwara, S. I. Yamazaki, M. Asahi, T. Nagai and T. Ioroi, *Electrochim. Acta*, 2015, **160**, 313–322.
32 J. Bisquert, G. Garcia-Belmonte, F. Fabregat-Santiago and A. Compte, *Electrochem. Commun.*, 1999, **1**, 429–435.
33 P. Gorai, T. Famprikis, B. Singh, V. Stevanović and P. Canepa, *Chem. Mater.*, 2021, **33**, 7484–7498.
34 B. Tjaden, S. J. Cooper, D. J. Brett, D. Kramer and P. R. Shearing, *Curr. Opin. Chem. Eng.*, 2016, **12**, 44–51.
35 Z. Wu and M. Liu, *Solid State Ionics*, 1996, **93**, 65–84.
36 D. S. McLachlan, *Mater. Res. Soc. Symp. Proc.*, 1996, **411**, 309–320.
37 D. S. McLachlan, M. Blaszkiewicz and R. E. Newnham, *J. Am. Ceram. Soc.*, 1990, **73**, 2187–2203.
38 D. A. G. Bruggeman, *Ann. Phys.*, 1935, **24**, 636–663.
39 R. Koerver, I. Aygün, T. Leichtweiß, C. Dietrich, W. Zhang, J. O. Binder, P. Hartmann, W. G. Zeier and J. Janek, *Chem. Mater.*, 2017, **29**, 5574–5582.
40 Y. Ma, J. H. Teo, D. Kitsche, T. Diemant, F. Strauss, Y. Ma, D. Goonetilleke, J. Janek, M. Bianchini and T. Brezesinski, *ACS Energy Lett.*, 2021, **6**, 3020–3028.
41 R. Tian, S. H. Park, P. J. King, G. Cunningham, J. Coelho, V. Nicolosi and J. N. Coleman, *Nat. Commun.*, 2019, **10**, DOI: 10.1038/s41467-019-09792-9.
42 P. Minnmann, F. Strauss, A. Bielefeld, R. Ruess, P. Adelhelm, S. Burkhardt, S. L. Dreyer, E. Trevisanello, H. Ehrenberg, T. Brezesinski, F. H. Richter and J. Janek, *Adv. Energy Mater.*, 2022, **12**, 2201425.
43 E. Schlautmann, A. Weiß, O. Maus, L. Ketter, M. Rana, S. Puls, V. Nickel, C. Gabbey, C. Hartnig, A. Bielefeld and W. G. Zeier, *Adv. Energy Mater.*, 2023, **13**, 1–9.
44 T. A. Hendriks, M. A. Lange, E. M. Kiens, C. Baeumer and W. G. Zeier, *Batteries Supercaps*, 2023, **6**, 202200544.